Yuan Xinyi (Orcid ID: 0000-0001-7147-3380)

Jin Fei Fei (Orcid ID: 0000-0001-5101-2296)

Zhang Wenjun (Orcid ID: 0000-0002-6375-8826)

A Concise and Effective Expression Relating Subsurface Temperature to the Thermocline in the Equatorial Pacific

Xinyi Yuan[1], Fei-Fei Jin[2*], Wenjun Zhang[1*]

[1]CIC-FEMD/ILCEC, Key Laboratory of Meteorological Disaster of Ministry of Education (KLME), Nanjing University of Information Science and Technology, Nanjing, China

[2]Department of Atmospheric Sciences, SOEST, University of Hawai‘i at Mānoa, Honolulu, HI, USA

Corresponding authors: Fei-Fei Jin (jff@hawaii.edu); Wenjun Zhang (zhangwj@nuist.edu.cn)

Key Points

- The equatorial Pacific subsurface temperature is expressed as a hyperbolic tangent function of thermocline depth and sharpness.
- Effective parameterizations for the subsurface temperature are derived by simple approximations of the thermocline sharpness.
- These parameterizations can be useful tools for evaluating the impacts of thermocline feedback on ENSO.

This article has been accepted for publication and undergone full peer review but has not been through the copyediting, typesetting, pagination and proofreading process which may lead to differences between this version and the Version of Record. Please cite this article as doi: 10.1029/2020GL087848

Abstract

The temperature of the subsurface water entrained into the surface mixed layer plays a key role in controlling the sea surface temperature (SST) and its interannual variability in the equatorial Pacific. In this paper, we combine a hyperbolic tangent function bounded by the warm pool SST and centered at the thermocline depth with a variable sharpness parameter to describe the time-space evolutions of the subsurface temperature. Under simple approximations of the sharpness parameter, this concise expression becomes remarkably efficient in capturing the observed and climate-model simulated subsurface temperature variability in terms of anomalies of the thermocline depth and SST of the El Niño-Southern Oscillation (ENSO) phenomenon. The formulations for the subsurface temperature and thermocline sharpness developed in this work should be useful tools for evaluating and understanding the role of the thermocline feedback in ENSO behaviors in both theoretical and comprehensive climate models.

Plain Language Summary

While significant advances have been made in our ability to understand, simulate, and predict the El Niño-Southern Oscillation (ENSO), its remarkable complexity is still not well understood. The subsurface ocean temperature in the equatorial Pacific is known to play a key role in controlling sea surface temperature and its interannual variations. An accurate description of its relationship with thermocline depth variability is of essential importance to understanding ENSO's complex dynamics in mechanistic studies. In this paper we develop a concise expression which captures the observed relationship between anomalies of the subsurface temperature and thermocline depth remarkably well. This expression should be useful for ENSO mechanistic model studies and diagnostic investigations into climate

models' performances in their ENSO simulations.

1. Introduction

Strong coupled ocean-atmosphere interactions in the tropical Pacific play an important role in forming its mean climate state, which is characterized by a strong warm pool and cold tongue temperature contrast, as well as in generating its interannual variability, which is dominated by the El Niño-Southern Oscillation (ENSO) phenomenon (Bjerknes, 1969; Cane & Zebiak, 1985; Jin, 1996, hereafter JIN96; Jin, 1998). ENSO exerts powerful global influence by reorganizing weather and climate patterns worldwide (Philander, 1983; Wallace et al., 1998; Alexander et al., 2002; McPhaden et al., 2006; Zhang et al., 2014, 2015). Decades of research around the world have yielded remarkable progress in understanding, simulating, and predicting the basic features of ENSO (e.g., Cane et al., 1986; Zebiak & Cane, 1987, hereafter ZC87; Chen et al., 1995, 2004; Jin, 1997; Neelin et al., 1998; Latif et al., 2001; Chen & Cane, 2008; Guilyardi et al., 2009; Taylor et al., 2012; Bellenger et al., 2014). The successful development of an effective hierarchical modeling approach has been instrumental to these advances. The Cane-Zebiak (CZ) model, which is in the middle of the hierarchical modeling chain, plays a key role in the understanding of basic ENSO dynamics. Nevertheless, it remains a major challenge to understand, simulate, and predict the rich features of ENSO, due to its temporal and spatial complexity (Timmermann et al., 2018). Further improving CZ-type models with better depiction of key physical processes may open a path for advancing our understanding of the dynamics of the ENSO complexity.

One of the crucial physical processes in CZ-type models involves the thermocline feedback, which depends heavily on the relationship between the temperature of the subsurface water entrained into the surface mixed layer, and the thermocline depth driven by the ENSO associated wind (DeWitte et al., 2002; Zhang & Zebiak, 2004). The ocean dynamic

adjustment for the thermocline depth's response to the surface wind is well demonstrated by theoretical and intermediate coupled CZ-type models (e.g., ZC87; JIN96; Jin, 1998). However, accurately describing the subsurface temperature that dictates the thermocline feedback remains a challenge. Previous studies have used local and nonlocal empirical parameterizations to establish a relationship between the subsurface temperature anomalies and the thermocline depth or ocean sea level anomalies (ZC87; J96; Kang & Kug, 2000; Keenlyside, 2001; Zhang et al., 2003, 2005; Zheng et al., 2006). Despite the usefulness of the parameterized relationships assumed or obtained in these studies, their validity has not been adequately substantiated. As ENSO's linear and nonlinear dynamics are sensitive to the strength of the thermocline feedback (e.g., Jin & Neelin, 1993), further research for this crucial relationship is warranted.

In this paper, we adopt a formulation that expresses the subsurface ocean temperature in terms of thermocline depth anomalies based on the approach used in JIN96, which has its roots in ZC87. In particular, the three-dimensional evolution of tropical Pacific ocean subsurface temperature is expressed via a simple hyperbolic tangent function centered at the 20°C depth with two parameters: the thermocline sharpness and warm pool SST; with the latter serving as the upper bound of the function. Our results show that this simple expression accurately describes the time-space evolution of subsurface temperature in the equatorial Pacific basin in observations or climate model simulations. Moreover, with simple approximations of the sharpness parameter, this concise expression yields remarkably effective parameterization schemes for subsurface temperature variability in terms of anomalies of the thermocline depth and SST, nicely capturing the nonlinear and nonlocal relationships exhibited during ENSO events. Our parameterization can be regarded as a constructive revision to the scheme built in ZC87 with which the results are also compared.

2. Data and Methodology

2.1 Datasets

We used the Phase 3.3.1 of the Simple Ocean Data Assimilation (SODA 3.3.1) monthly reanalysis from 1980–2015 provided by the US University of Maryland (Carton et al., 2018); the horizontal resolution was linearly interpolated to 5.625°×2°, as in the CZ model. Two additional monthly reanalysis datasets with horizontal resolution linearly interpolated to 1°×1° were used to demonstrate the universal applicability of our formulation. The two datasets are: European Centre for Medium Range Weather Forecasts (ECMWF) Ocean Reanalysis System 5 (ORAS5) (Zuo et al., 2019) from 1979–2018; and Global Ocean Data Assimilation System (GODAS) (Behringer & Xue, 2004) from 1980–2018. To further examine the universality of our formulation, we apply it to the output of the pre-industrial control (piControl) simulations from the Geophysical Fluid Dynamics Laboratory (GFDL) Climate Model version 3 (GFDL-CM3), participating in the Coupled Model Intercomparison Project Phase 5 (CMIP5) (Taylor et al., 2012). The vertical structures are all linearly interpolated at 10 m interval for the upper 400 m of the tropical Pacific.

2.2 Methodology: A functional expression for the subsurface temperature

Observed subsurface temperature always has sharp transitions through the thermocline; this thermal structure was first described in ZC87 using a hyperbolic tangent function to relate subsurface temperature anomalies to thermocline anomalies and was assumed to move intact without stretching following the thermocline going up or down. JIN96 adopted the same assumption and used this function to describe total subsurface temperature. Following the same formulation as in JIN96, the three-dimensional subsurface temperature evolution is expressed as follows.

$$T_{sub} = T_r - (T_r - 20)(1 - \tanh\frac{h - z}{h^*}) \quad (1)$$

Here h denotes the thermocline depth, which is defined as the depth of the 20°C isotherm,

and depth z increases downward. The vertical distributions of subsurface temperature above and below z=h depend on parameters h^* and T_r, which control the sharpness of thermocline and the upper bound of the subsurface temperature, respectively. Following JIN96, we use the Pacific warm pool SST for T_r and set it at 30°C. Equation (1) will work for the entire upper ocean up to a depth of about 300–350 meters, when the function hits the low bound at 10°C.

The sharpness parameter in JIN96 was set at a constant 50 m; subsequently this critical parameter has never been carefully examined using observational data. We here propose a method to derive this parameter for the reanalysis datasets, or any comprehensive climate model output, by inverting the function in Eq. (1) to calculate h^* as follows.

$$h^* = (h - z) / \arctan\mathrm{h}\left(\frac{T^o_{sub} - 20}{T_r - 20}\right) \tag{2}$$

Here T^o_{sub} is the observed or simulated time-space evolution of the subsurface temperature. The calculation of h^* will encounter numerical difficulty when the absolute value of z-h is near zero (or significantly less than 10 m in practice). In the region |z-h|≤10m, we find h^* by taking the derivative of Eq. (1) with respect to z and evaluate the result at z=h as follows:

$$h^* = -(T_r - 20) / \left.\frac{\partial T^o_{sub}}{\partial z}\right|_{z=h} \tag{3}$$

Equations (2–3) allow a complete determination for local sharpness with full time-space dependence.

The climatological mean distribution of $\overline{h^*}$ as shown in Fig. 1a is calculated using the monthly climatological subsurface temperature $\overline{T}_{sub}$ and thermocline depth $\overline{h}$ in Eqs. (2–3). Note that with this definition of $\overline{h^*}$, calculating $\overline{T}_{sub}$ using Eq. (1) describes observed climatological subsurface temperature exactly. Interestingly, except in regions far below the cold tongue and in the far west under the warm pool, $\overline{h^*}$ is almost uniform and is about 60m

(Fig. S1a, c). It has a weak minimum near z=$\overline{h}$, as expected from Eq. (3). There are small meridional and zonal variations in the equatorial region (Fig. S1) and a weak seasonal cycle mainly at 50-75m depth (Fig. S2). Moreover, the full time-space dependent h^* derived from the observed T_{sub}^o exhibits modest interannual variations (Fig. 1b). The standard deviation is about 20m, mainly in the upper thermocline near the surface layer. Eqs. (2-3) thus provide a well-defined thermocline local sharpness which can be readily diagnosed from reanalysis datasets or any climate model outputs. Because observed h^* has relatively modest variability, we propose to consider two zeroth-order and one first-order approximations to parameterize h^* as follows.

(a1) $h^* \approx 60\ m$

(a2) $h^* \approx \overline{h^*}(x,y,z)$

(b) $h^* \approx \overline{h^*}(x,y,z) + \hat{h}^{*'}$

Here $\hat{h}^{*'}$ is an approximation of anomalous sharpness $h^{*'} = h^* - \overline{h^*}$ through a multiple linear regression, as follows.

$$\hat{h}^{*'} = b(x,y,z)h'(x,y,t) + e(x,y,z)T'(x,y,t) \quad (4)$$

Here, b and e are regression coefficients, calculated for each 5° x 5° x 10m box. The two variables, h' and T' denote monthly anomalies of thermocline depth and mixed-layer SST. The regression coefficient e is largely concentrated near z=50m as it reflects the impact of SST on $\hat{h}^{*'}$ through the entrainment process near the mixed layer. To eliminate the small inconsequential but spurious values in this coefficient at deep depth, we apply an additional factor $\exp[-(\frac{z-50}{50})^2]$ to the regression coefficient e so that SST's impact on $\hat{h}^{*'}$ is limited in the upper thermocline. This linear approximation captures a substantial part of thermocline sharpness and displays almost same results in different periods (Fig. S3).

The hyperbolic tangent functional transformation in Eqs. (1–3) makes otherwise nonlocal and nonlinear relationships among subsurface temperature, thermocline, and SST easily determinable through simple and robust approximations to thermocline sharpness. Applying the three approximations for h^* to Eq. (1), we have three different parameterization schemes for subsurface temperature anomalies:

$$
\begin{aligned}
&A1) \quad T'_{sub} = (T_r - 20)\left(\tanh\frac{\overline{h} - z + h'}{60} - \tanh\frac{\overline{h} - z}{60}\right) \\
&A2) \quad T'_{sub} = (T_r - 20)\left(\tanh\frac{\overline{h} - z + h'}{\overline{h^*}} - \tanh\frac{\overline{h} - z}{\overline{h^*}}\right) \\
&B) \quad T'_{sub} = (T_r - 20)\left(\tanh\frac{\overline{h} - z + h'}{\overline{h^*} + bh' + eT'} - \tanh\frac{\overline{h} - z}{\overline{h^*}}\right)
\end{aligned}
\tag{5}
$$

Hereafter we will refer to them as scheme A1, A2 and B respectively. Scheme A1 is the same as the scheme proposed in JIN96; whereas A2 is an extension of A1 with the consideration of the climatological distributions of the sharpness. The underlying assumption of these two schemes is the same as in ZC87: all subsurface vertical temperature profiles are assumed to be shape-preserved, and to move up and down with the varying thermocline depth. There is not any regression used in these two cases because h^* is determined simply based on the observed climatological subsurface temperature field.

In addition to the basic assumptions of ZC87 and scheme A1 and A2, the subsurface vertical temperature profiles in scheme B further includes modest sharpness variations that depend on ENSO SST and thermocline anomalies through a linear regression. The impact of SST on the sharpness may be related to the mixing process, whereas the physical processes for thermocline depth to affect sharpness remain unclear. This consideration allows a modest asymmetric dependence of the subsurface temperature on the thermocline depth and more accurate results than scheme A1 and A2, at the cost of introducing two additional empirical parameters.

For comparison, we list the ZC87 parameterization for the subsurface temperature

anomaly at z=50 m

$$T_{sub}^{'} = \begin{cases} T_1 \left\{ \tanh[b_1(\bar{h}+h^{'})] - \tanh(b_1\bar{h}) \right\}, & h^{'} > 0 \\ T_2 \left\{ \tanh[b_2(\bar{h}-h^{'})] - \tanh(b_2\bar{h}) \right\}, & h^{'} < 0 \end{cases} \quad (6a)$$

and entrained ocean temperature anomaly at z=50 m as

$$T_e^{'} = \gamma T_{sub}^{'} + (1-\gamma)T^{'} \quad (6b)$$

The formulations in Eqs. (6a) and (6b) will be referred hereafter as ZC87-a and b, respectively. The two fitting parameters in ZC87-a were set as (T_1, b_1) for the positive phase (El Niño) and (T_2, b_2) for the negative phase (La Niña) of subsurface temperature anomalies. These parameters were obtained through nonlinearly fitted using very limited observational data available nearly four decades ago. They were set as (28°C, 1/(80 m)) and (-40°C, 1/(33 m)), respectively, whereas the entrainment parameter γ in ZC87-b was set at 0.75. JIN96 adopted ZC87's choice of the hyperbolic tangent function and formulated the total subsurface temperature, also using two parameters. However, these two parameters were set as the warm pool SST and a constant thermocline sharpness without any discontinuous distinction according to ENSO phases. The JIN96 formulation, as generalized in Eqs. (1–3), allows for a straightforward determination of the upper bound of subsurface temperature and a precise determination of the local sharpness of the thermocline from data. While schemes A1 and A2 have the same basic assumption as ZC87-a, the inclusion of the SST effect on the subsurface temperature anomalies in scheme B may be viewed as conceptually equivalent to the consideration in ZC87-b. Our formulation for three-dimensional subsurface temperature anomalies (Eq. (5)) can be regarded as a constructive revision to the formulation of ZC87. In next section, we will demonstrate that the hyperbolic tangent formulation ingeniously envisioned in ZC87 and extended in schemes A1, A2 and B is highly effective at describing the subsurface ocean temperature.

3. Results

We first examine the performance of the parameterization schemes in Eq. (5) in capturing the vertical distributions and profiles of subsurface temperature. We focus on ENSO composites (Fig.2), because the climatological three-dimensional subsurface temperature is, by-definition, captured by the given two-dimensional climatological thermocline depth and three-dimensional climatological thermocline sharpness, with only a negligible difference due to the coarse grid calculation of the thermocline sharpness (Fig. S4c). The ENSO events participating in the composite are based on the Oceanic Niño Index (ONI) in the Niño 3.4 region (5°N-5°S, 120°-170°W) during their peak phase (November-December-January, NDJ) according to the definition by the Climate Prediction Center. The parameterized vertical distributions of the subsurface ocean temperature are in reasonable agreements with the observation even for the simplest scheme A1 (Fig. 2a, b). In terms of z-h vertical coordinates, the simplest scheme A1 has one universal vertical profile of subsurface ocean temperature at different longitudes (Fig. 2c, d). It can be seen that the dash-profiles in Fig. 2c and 2d follow the same profile, and they differ only due to different ranges of z-h at different longitudes. Near the thermocline depth (z-h=0), the observed vertical profiles in different longitudes are very similar to the universal vertical profile (Fig. 2c, d). There is some bias near surface and in the deep region under the cold tongue (Fig. 2a-d and Fig. S4a-b) because of the large difference between the observed climatological value and the assumed value (60m) of the thermocline sharpness in scheme A1. This bias disappears in scheme A2 when climatological field of the thermocline sharpness is used (Fig. 2e-f and Fig. S4c). Compared with scheme A1, scheme A2 eliminates the large bias in deep depth and yields a modest improvement in the upper thermocline. Scheme B, further including the sharpness variations due to SST entrainment and thermocline dynamic effects, captures the vertical distribution of subsurface ocean temperature most accurately among the three schemes (Fig.

2g-h).

We also examine the most extreme cases of the 1997–1999 El Niño and La Niña peak phases (Fig. S5). Schemes A1 and A2 show significant bias near the top of the profiles (Fig. S5a-f) where subsurface temperature anomalies matter the most for their influence on SST anomalies. In comparison, scheme B is much better at capturing the vertical profiles (Fig. S5g-h) in these extreme cases. We also notice that omitting the h' dependence term in the sharpness gives rise to similar results with those from scheme B (not shown), indicating that the entrainment effect dominates in the gained accuracy in the upper thermocline for scheme B.

Because the horizontal pattern of subsurface temperature below and near the mixed layer at 50m is of great importance in determining ENSO SST anomalies through upwelling and entrainment processes, we further compare the observed and parameterized patterns using scheme B for different types of ENSO at these depths as shown in Fig. 3. Here, we identify EP/CP ENSO events using the methods of Zhang et al. (2014, 2015, 2019), which distinguish two types for both El Niño and La Niña events. The events comprising the EP El Niño composite are 1982/83, 1997/98, and 2015/16; the CP El Niño events are 1994/95, 2002/03, 2004/05, 2009/10, and 2014/15; the EP La Niña events are 1984/85, 1995/96, 1999/00, 2005/06, and 2007/08; the CP La Niña events are 1988/89, 1998/99, 2000/01, 2010/11, and 2011/12. Some ENSO events are not included in our consideration due to their mixed features. As shown in Fig. 3, scheme B performs well in capturing the horizontal patterns of the subsurface temperature at 50 m. During the peak phase of El Niño, positive subsurface temperature anomalies occupy the central and eastern equatorial Pacific, and some negative anomalies exist in the western to northern equatorial Pacific (Fig. 3a, d). This pattern is roughly opposite of that during the La Niña peak phase (Fig. 3g, j). The warm and cold phases display a strong asymmetry of the subsurface temperature in the amplitude. The

amplitude of EP El Niño is generally much larger than that of EP La Niña (Fig. 3a, g), while the CP El Niño's amplitude is slightly weaker than that of CP La Niña (Fig. 3d, j). It is interesting to note that ENSO subsurface temperature anomaly patterns exhibit less contrast between the EP and CP events, which is very different from their high contrast SST anomaly patterns. This notion is consistent with previous arguments that emphasized the effect of the enhanced zonal advective feedback for the CP events (Kug et al., 2009; Ren & Jin, 2013). Overall, our formulation achieves very good performance in capturing the main features of the subsurface temperature fields (Fig. 3b, e, h, k). The substantial under-parameterization for the subsurface temperature anomalies of La Niña events in the ZC87 parameterization is eliminated in our scheme B. The results at z=75m are similar and even have slightly better agreement with observation (not shown).

We also examined its variance and skewness (Fig. 3m, n) from the equatorial time evolution of the parameterized and observed subsurface temperature (Fig. S6) at z=50m. Once again, scheme B performs well in capturing the observed evolution of subsurface temperature anomalies and the observed variance and skewness in the eastern equatorial Pacific, where the subsurface temperature anomalies matter most for ENSO because of their strong impact on SST anomalies. Compared to A1 and A2 (not shown), scheme B clearly performs better as a result of including sharpness variations.

The results from applying various ENSO composites, extreme events, evolutions, variance and skewness of subsurface temperature anomalies, demonstrate a solid validation for the hyperbolic tangent formulation envisioned in ZC87 and JIN96. Schemes A1, A2 and B, with their progressively greater complexity and accuracy, are all highly efficient for capturing the vertical profiles in different locations and different ENSO phases. They may be useful for mechanistic models of different complexity for ENSO studies.

Our subsurface temperature parameterization scheme can be applied to any reanalysis

data without need for parameter adjustment. Indeed, ENSO subsurface temperature anomalies are well represented by our formulation, not only for SODA data but for other datasets as well (e.g., ORAS5 and GODAS datasets) as shown in Fig. S7a. We also applied our parameterization to the output of CMIP5 climate model simulations and it is equally effective; the climatological sharpness and the regression coefficients for sharpness anomalies are derived based on each model's output. An example for the GFDL-CM3 pre-industrial control simulation is shown in Fig. S7b. The model-simulated subsurface temperature anomalies and the model-data based parameterization using scheme B are nearly identical. Further investigations using our scheme to assess the simulation skill for the ENSO thermocline feedback in General Circulation Models and the sensitivity of simulated subsurface temperature anomalies to anomalies in thermocline depth and SST will be reported in near future.

To elucidate the longitudinal dependence of the nonlinear relationship between subsurface temperature anomalies and thermocline depth anomalies, we show the scatter diagrams in Fig. 4. The slopes reflect the sensitivity of subsurface temperature anomalies to thermocline depth anomalies and control the strength of the ENSO thermocline feedback. Sensitivity decreases westward, which is captured by our formulation. ZC87 performs well at 90°W but its performance degrades at other longitude bands. It is evident from the near equal slopes between ENSO warm and cold phases (Fig. 4a-c) that warm and cold event asymmetry in subsurface temperature is not the result of asymmetric sensitivities to the thermocline depth anomaly. Instead, it largely comes from the asymmetry of thermocline depth anomalies themselves. This is true both in observations and in our formulation (Fig. 4d-f). In contrast, ZC87-b has built-in asymmetric sensitivities of subsurface temperature to the thermocline depth anomaly as the results of the built-in discontinuous slopes: a strong slope for the El Niño phase and a much weaker slope for La Niña (Fig. 4g-i). This feature is clearly not

supported by reanalysis data, which were not available to the authors of ZC87. How this built-in asymmetry sensitivities, which cause excess skewness of subsurface temperature anomalies as seen in Fig. 3, affect the ENSO asymmetry simulated in the CZ model is worthy of further investigation. That topic is beyond the scope of this paper but will be pursued in the near future.

4. Summary and Discussion

In this paper, we provided supporting evidence for, and provided a new formulation of a hyperbolic tangent expression for the subsurface temperature in terms of the thermocline depth in the equatorial Pacific as proposed by ZC87 and JIN96. Based on the formulation of JIN96, we establish the definition of the thermocline sharpness and derive a method to determine its time-space evolutions. With knowledge of the observed thermocline sharpness, we propose three subsurface temperature parameterization schemes with progressive complexity. We demonstrated that our new formulations capture both the observed climate mean state and ENSO-associated variability very well.

Our schemes may be used in the CZ-type mechanistic ENSO models that played a key role in advancing the ENSO theory for the past three decades (Jin et al., 2020). Further investigations applying the schemes developed in this work to a hierarchical ENSO modeling may lead to better understanding of the fundamental dynamics of ENSO, and more accurate simulations and predictions of ENSO as well.

Acknowledgments

We would like to thank Prof. Mark Cane for his insightful review, which led the senior author of this paper to refine the formulations for completeness and clarity, as well as led to significantly improved results, and Prof. Christina Karamperidou for valuable comments and

editing on the revised manuscript. We also thank Dr. J.-X. Zhao, S. Zhao, and L. Geng, A. Xue and C. Liu for their comments on earlier versions of manuscripts. We highly appreciate SOEST editorial support from Ms. May Izumi. This work is supported by the National Key Research and Development Program (2018YFC1506002), the National Nature Science Foundation of China (41675073). F.-F. Jin was supported by the U.S. National Science Foundation (AGS-1406601 and AGS-1813611) and the U.S. Department of Energy Grant (DE-SC0005110). The SODA3.3.1 data is available at https://www2.atmos.umd.edu/~ocean/index_files/soda3.3.1_mn_download.htm; GODAS data is available at https://cfs.ncep.noaa.gov/cfs/godas/monthly/; and ECMWF ORAS5 data was downloaded from http://icdc.cen.uni-hamburg.de/thredds/catalog/ftpthredds/EASYInit/oras5/catalog.html. The output of the piControl simulation from GFDL-CM3 was downloaded from https://cera-www.dkrz.de/WDCC/ui/cerasearch/entry?acronym=NGG3pcMOOthetao111v110601.

References

Alexander, M. A., Blade I., Newman M., Lanzante J. R., Lau N. C., & Scott J. D. (2002). The atmospheric bridge: the influence of ENSO teleconnections on air-sea interaction over the global oceans. *Journal of Climate, 15*(6), 2205–2231. https://doi.org/10.1175/1520-0442(2002)015<2205:TABTIO>2.0.CO;2

Behringer, D., & Xue, Y. (2004). Evaluation of the global ocean data assimilation system at NCEP: The Pacific Ocean. Paper presented at Eighth Symposium on Integrated Observing and Assimilation Systems for Atmosphere, Ocean, and Land Surface. American Meteorological Society 84th Annual Meeting, Seattle, WA.

Bellenger, H., Guilyardi, E., Leloup, J., Lengaigne, M., & Vialard, J. (2014). ENSO representation in climate models: from CMIP3 to CMIP5. *Climate Dynamics, 42*, 1999–2018. https://doi.org/10.1007/s00382-013-1783-z

Bjerknes, J. (1969). Atmospheric teleconnections from the equatorial Pacific. *Monthly Weather Review, 97*(3), 163–172. https://doi.org/10.1175/1520-0493(1969)097,0163:ATFTEP.2.3.CO;2

Cane, M. A., & Zebiak, S. E. (1985). A theory for El Niño and the Southern Oscillation. *Science, 228*(4703), 1085–1087. https://doi.org/10.1126/science.228.4703.1085

Cane, M. A., Zebiak, S. E., & Dolan, S. C. (1986). Experimental forecast of El Niño. *Nature, 321*, 827–832. https://doi.org/10.1038/321827a0

Carton, J. A., Chepurin, G. A., & Chen, L. (2018). SODA3: a new ocean climate reanalysis, *Journal of Climate, 31*, 6967–6983. https://doi.org/10.1175/JCLI-D-18-0149.1

Chen, D., Zebiak, S. E., Busalacchi, A. J., & Cane, M. A. (1995). An improved procedure for El Niño forecasting: Implications for predictability. *Science, 269*(5231), 1699–1702. https://doi.org/10.1126/science.269.5231.1699

Chen, D., Cane, M. A., Kaplan, A., Zebiak, S. E., & Huang, D. (2004). Predictability of El Niño over the past 148 years. *Nature, 428*, 733–736. https://doi.org/10.1038/nature02439

Chen, D., & Cane, M. A. (2008). El Niño prediction and predictability. *Journal of Computational Physics, 227*(7), 3625–3640. https://doi.org/10.1016/j.jcp.2007.05.014

DeWitte, B., Gushchina, D., duPenhoat, Y., & Lakeev, S. (2002). On the importance of subsurface variability for ENSO simulation and prediction with intermediate coupled models of the tropical Pacific: A case study for the 1997–1998 El Niño. *Geophysical Research Letters, 29*, 1666. https://doi.org/10.1029/2001GL014452

Guilyardi, E., Wittenberg, A., Fedorov, A., Collins, M., Wang, C. Z., Capotondi, A., et al. (2009). Understanding El Niño in ocean-atmosphere general circulation models: progress and challenges. *Bulletin of the American Meteorological Society, 90*, 325–340. https://doi.org/10.1175/2008BAMS2387.1

Jin, F.-F., & Neelin, J. D. (1993). Modes of Interannual Tropical Ocean-Atmosphere Interaction - a Unified View. Part I: Numerical results.*Journal of the Atmospheric Sciences, 50*, 3477–3503. https://doi.org/10.1175/1520-0469(1993)050<3477%3AMOITOI>2.0.CO%3B2

Jin, F.-F. (1996). Tropical ocean-atmosphere interaction, the Pacific cold tongue, and the El Niño Southern Oscillation. *Science, 274*(5284), 76–78. https://doi.org/10.1126/science.274.5284.76

Jin, F.-F. (1997). An equatorial ocean recharge paradigm for ENSO. Part I: Conceptual model. *Journal of the Atmospheric Sciences, 54*, 811–829. https://doi.org/10.1175/1520-0469(1997)054<0811:AEORPF>2.0.CO;2

Jin, F.-F. (1998). A simple model for the Pacific cold tongue and ENSO. *Journal of the Atmospheric Sciences, 55*, 2458–2469. https://doi.org/10.1175/1520-0469(1998)055<2458:ASMFTP>2.0.CO;2

Jin, F.-F., Chen, H.-C., Zhao, S., Hayashi, M., Karamperidou, C., Stuecker, M. F., et al. (2020). Simple ENSO Models. In M. J. McPhaden, A. Santoso, W. Cai (Eds.), *El Niño Southern Oscillation in a Changing Climate, Geophysical Monograph Series* (Vol. 253, pp. 121–151). Washington, DC: American Geophysical Union.

Kang, I.-S., & Kug, J.-S. (2000). An El Niño prediction system using an intermediate ocean and a statistical atmosphere. *Geophysical Research Letters, 27*, 1167–1170. https://doi.org/10.1029/1999GL011023

Keenlyside, N. (2001). Improved modeling of zonal currents and SST in the tropical Pacific, (Doctoral dissertation). Monash University, Australia. https://doi.org/10.4225/03/59ca0575c5cf5

Kug, J.-S., Jin, F.-F., & An, S.-I. (2009). Two types of El Niño events: Cold tongue El Niño and warm pool El Niño. *Journal of Climate, 22*, 1499–1515. https://doi.org/10.1175/2008JCLI2624.1

Latif, M., Sperber, K., Arblaster, J., et al. (2001). ENSIP: The El Niño simulation intercomparison project. *Climate Dynamics, 18*, 255–276. https://doi.org/10.1007/s003820100174

McPhaden, M. J., Zebiak, S. E., & Glantz, M. H. (2006). ENSO as an integrating concept in Earth science. *Science, 314*(5806), 1740–1745. https://doi.org/10.1126/science.1132588

Neelin, J. D., Battisti, D. S., Hirst, A. C., Jin, F.-F., Wakata, Y., Yamagata, T., & Zebiak, S. E. (1998). ENSO theory. *Journal of Geophysical Research, 103*, 14262–14290. https://doi.org/10.1029/97JC03424

Philander, S. G. H. (1983). El Niño Southern Oscillation Phenomena. *Nature, 302*(5906), 295–301. https://doi.org/10.1038/302295a0

Ren, H. L., & Jin, F.-F. (2013). Recharge oscillator mechanisms in two types of ENSO. *Journal of Climate, 26*(17), 6506–6523. https://doi.org/10.1175/JCLI-D-12-00601.1

Taylor, K. E., Stouffer, R. J., & Meehl, G. A. (2012). An overview of CMIP5 and the experiment design. *Bulletin of the American Meteorological Society, 93*, 485–498. https://doi.org/10.1175/BAMS-D-11-00094.1

Timmermann, A., An, S.-I., Kug, J.-S., Jin, F.-F., Cai, W., Capotondi, A., et al. (2018). El Niño-Southern Oscillation complexity. *Nature, 559*, 535–545. https://doi.org/10.1038/s41586-018-0252-6

Wallace, J. M., Rasmusson, E. M., Mitchell, T. P., Kousky, V. E., Sarachik, E. S., & von Storch, H. (1998). On the structure and evolution of ENSO related climate variability in the tropical Pacific: Lessons from TOGA. *Journal of Geophysical Research, 103*(C7), 14241–14259. https://doi.org/10.1029/97JC02905

Zebiak, S. E., & Cane, M. A. (1987). A model El Niño–Southern Oscillation. *Monthly Weather Review, 115*(10), 2262–2278. https://doi.org/ 10.1175/1520-0493(1987)1152.0.CO;2

Zhang, R. H., Zebiak, S.E., Kleeman, R., & Keenlyside, N. (2003). A new intermediate coupled model for El Nino simulation and prediction. *Geophysical Research Letters, 30*(19), 2012. https://doi.org/10.1029/2003GL018010

Zhang, R. H., & Zebiak, S.E. (2004). An embedding method for improving interannual variability simulation in a hybrid coupled model of the tropical Pacific ocean-atmosphere system. *Journal of Climate, 17*, 2794–2812. https://doi.org/10.1175/1520-0442(2004)017<2794:AEMFII>2.0.CO;2

Zhang, R. H., Kleeman, R., Zebiak, S. E., Keenlyside, N., & Raynaud, S. (2005). An empirical parameterization of subsurface entrainment temperature for improved SST simulations in an intermediate ocean model. *Journal of Climate, 18*, 350–371. https://doi.org/10.1175/JCLI-3271.1

Zhang, W., Jin, F.-F., & Turner, A. (2014). Increasing autumn drought over southern China associated with ENSO regime shift. *Geophysical Research Letters, 41*, 4020–4026. https://doi.org/10.1002/2014GL060130

Zhang, W., Wang, L., Xiang, B., Qi, L., & He, J. (2015). Impacts of two types of La Niña on the NAO during boreal winter. *Climate Dynamics, 44*(5-6), 1351–1366. https://doi.org/10.1007/s00382-014-2155-z

Zhang, W., Wang, Z., Stuecker, M. F., Turner, A. G., Jin, F.-F., & Geng, X. (2019). Impact of ENSO longitudinal position on teleconnections to the NAO. *Climate Dynamics, 52*(1-2), 257–274. https://doi.org/10.1007/s00382-018-4135-1

Zheng, F., Zhu, J., Zhang, R. H., & Zhou, G. (2006). Ensemble hindcasts of SST anomalies in the tropical Pacific using an intermediate coupled model. *Geophysical Research Letters, 33*(19), L19604. https://doi.org/10.1029/2006GL026994

Zuo, H., Balmaseda, M. A., Tietsche, S., Mogensen, K., & Mayer, M. (2019). The ECMWF operational ensemble reanalysis-analysis system for ocean and sea ice: a description of the system and assessment. *Ocean Science, 15*, 779–808. https://doi.org/10.5194/os-15-779-2019

Figures

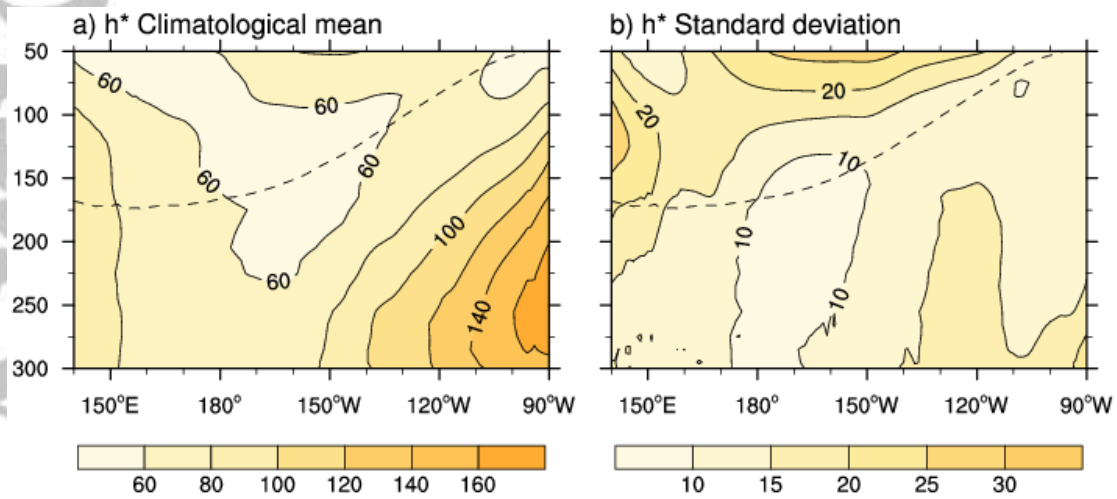

Figure 1. Climatological mean **(a)** and standard deviation **(b)** of the equatorial (5°S–5°N) thermocline sharpness h^* (m). Dashed lines denote the climatological mean depth of the thermocline.

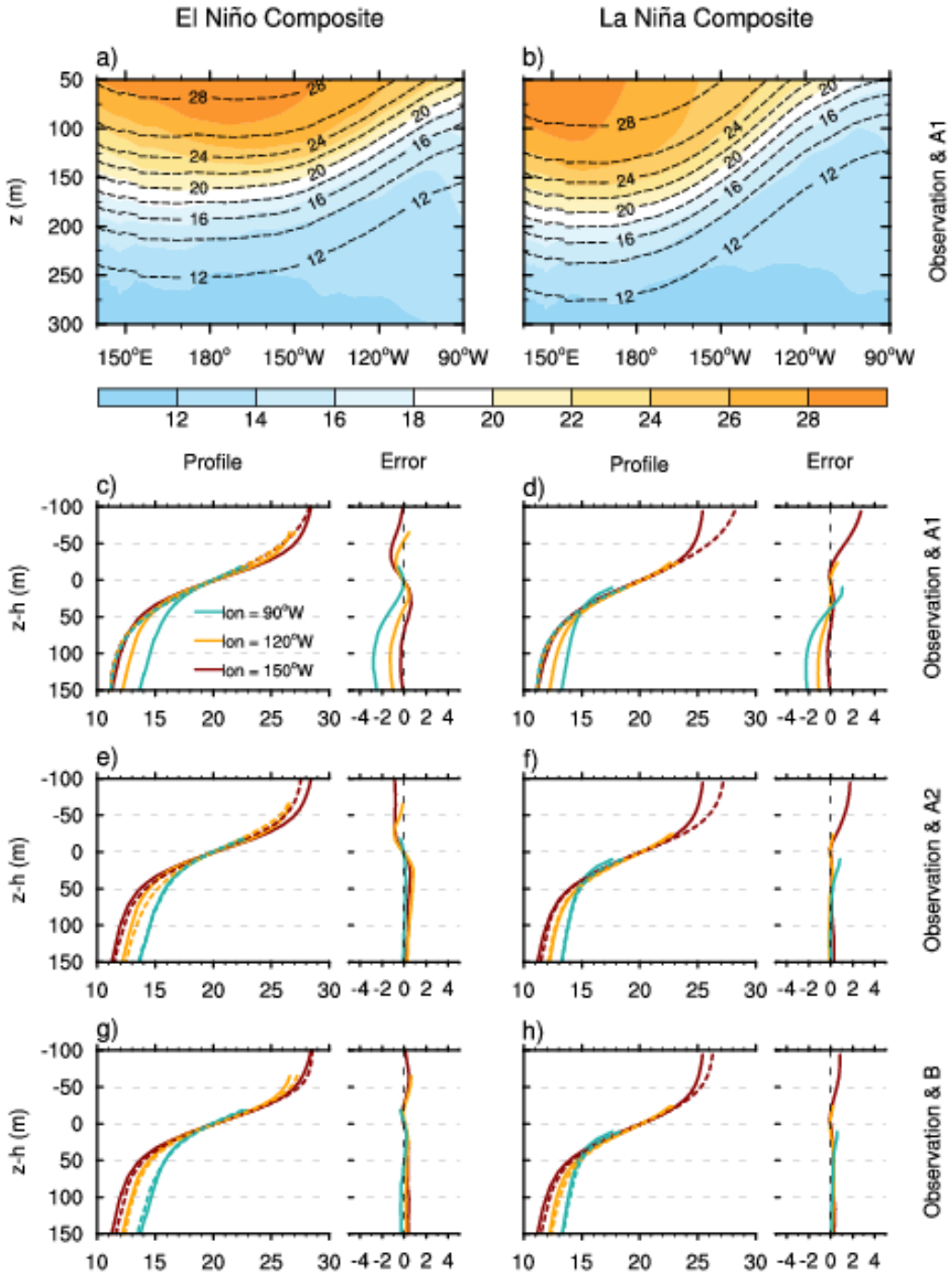

Figure 2. Vertical distributions of the equatorial (5°S–5°N) subsurface temperature for the peak phases (NDJ) of the El Niño events **(a)** and La Niña events **(b)** for the observations (shading) and scheme A1 parameterization (dashed contours). The observed (solid curves) and parameterized (dashed curves) vertical profiles of subsurface temperature (°C) for scheme A1 **(c, d)**, scheme A2 **(e, f)**, and scheme B **(g, h).** Panels in **(c, e, g)** are for El Niño events and **(d, f, h)** for La Niña events. Vertical profiles at different longitudes (90°W, 120°W, and 150°W) are color labeled. The solid curves in the right-hand panels of **(c-h)** show the errors in scheme A1, A2 and B respective to the observation.

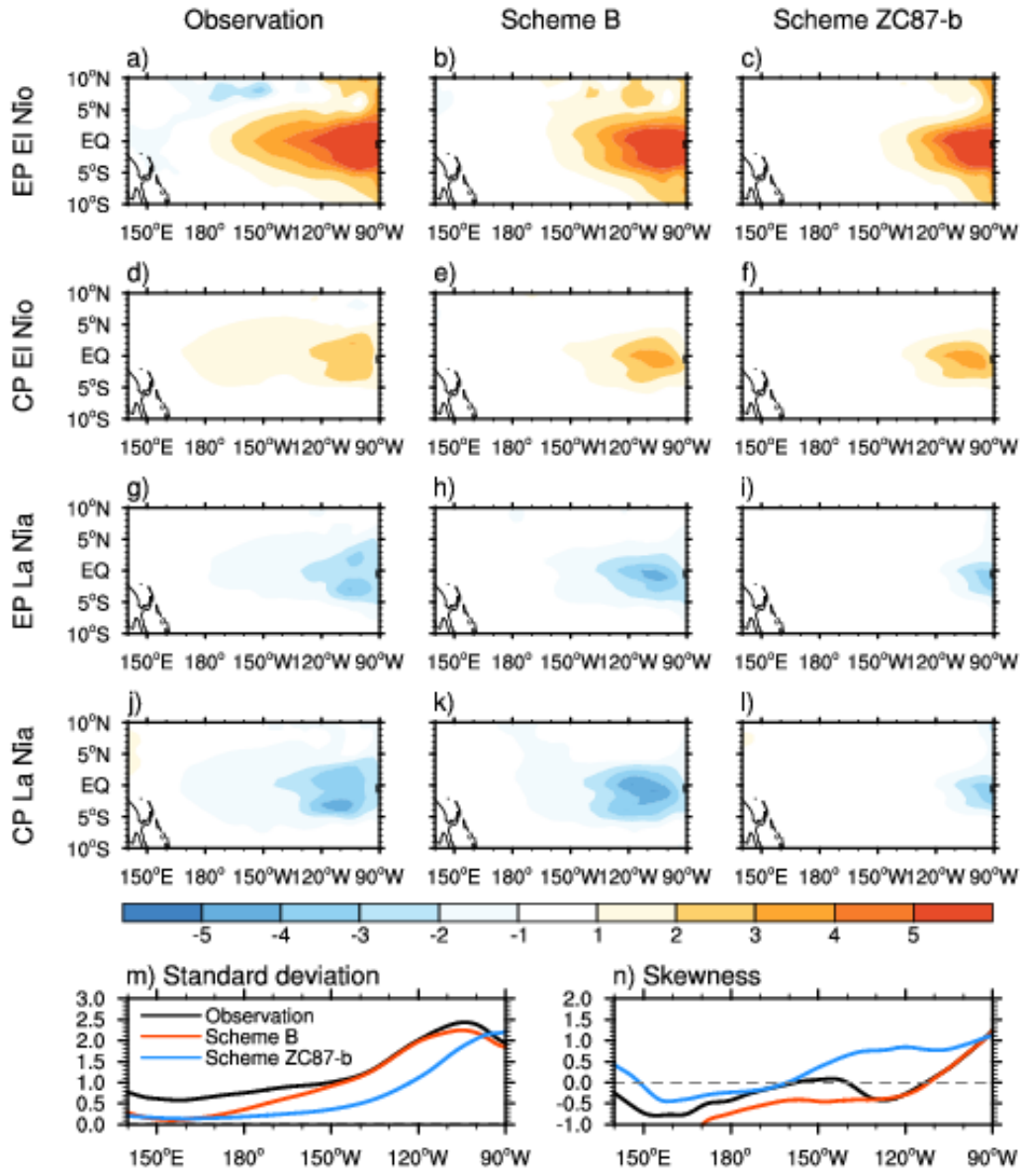

Figure 3. Composite patterns of the subsurface temperature anomalies (°C) at 50 m during the peak phases (NDJ) of the EP El Niño **(a–c)**, CP El Niño **(d–f)**, EP La Niña **(g–i)**, and CP La Niña **(j–l)** for the observation **(a, d, g, j)**, scheme B **(b, e, h, k)**, and scheme ZC87-b **(c, f, i, l)**. The standard deviation **(m)** and skewness **(n)** of the equatorial (5°S–5°N) subsurface temperature (°C) at 50 m for the observation (black curve), parameterization in scheme B (red curve), and scheme ZC87-b (blue curve).

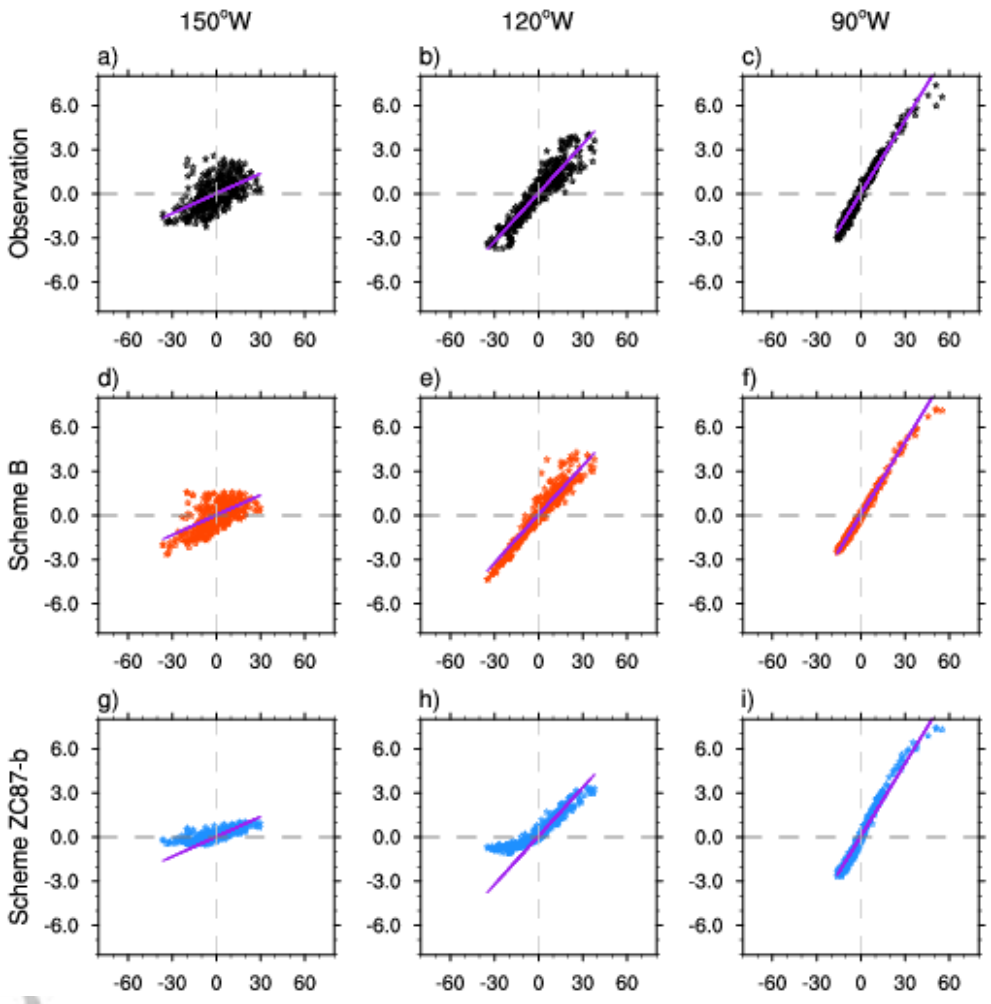

Figure 4. Scatter plots of the relationship between the subsurface temperature anomalies T'_{sub} (°C) at 50 m (y axis) and thermocline depth anomalies h' (m) (x axis) averaged in a band of 10 degrees of longitude at different longitudes of the equatorial Pacific (5°S–5°N) for the observation **(a–c)**, scheme B **(d–f)**, and scheme ZC87-b **(g–i)**. The purple lines denote the linear regression lines for observations.